Project Design Report

Miniature Ultrasound Probe for Direct Visualization in ERCP, 9 December 2024, BMED 4602,

Fall 2024

Advised by Dr. Raja R. Sappati Biyyani, MD, GI Specialists of Georgia

Louis Klem

Colten Palkon

Ashtyn Cauffman

Primary Editor: Shea Harrell

Table of Contents

Executive Summary

Endoscopic Retrograde Cholangiopancreatography (ERCP) is a vital procedure performed more than 600,000 times annually in the United States to diagnose and treat biliary and pancreatic duct conditions [1]. Despite its clinical importance, current duodenoscopes have significant limitations in providing adequate visualization during selective cannulation. These limitations contribute to complications such as pancreatitis, infection, bleeding, and swelling of the papilla, which can lead to failed cannulation and necessitate repeat procedures. Such outcomes increase patient morbidity, extend procedural times, and add to healthcare costs [2].

The ER-SEE-P device addresses these challenges by providing gastroenterologists with direct visualization of the duodenal papilla through the integration of forward-viewing ultrasound technology. This innovative device enables precise guidewire placement while reducing the risks of tissue trauma and minimizing reliance on fluoroscopy. The ultrasound imaging system delivers high-resolution visuals with a depth penetration of at least 1.5 cm, ensuring anatomical clarity. The device is constructed from biocompatible, low-friction materials to minimize tissue abrasions and is designed to integrate seamlessly with standard workflows.

The primary users of the ER-SEE-P are gastroenterologists performing ERCP procedures, supported by surgical assistants and healthcare staff responsible for device setup and operation. Healthcare institutions serve as the primary clients, as the device offers a cost-effective means to improve procedural outcomes, reduce complications, and enhance overall safety for both patients and clinicians. By addressing these critical needs, the ER-SEE-P positions itself as a transformative tool that aligns with the growing demand for safer and more effective gastrointestinal endoscopic devices.

Project Description

The ER-SEE-P device addresses the significant clinical challenges faced by gastroenterologists that perform endoscopic retrograde cholangiopancreatography (ERCP). Current side-viewing duodenoscopes provide limited visualization of the duodenal papilla, resulting in complications such as tissue trauma, pancreatitis, infection, and swelling. These issues often lead to failed cannulation, necessitating repeat procedures, which further increase patient risks and healthcare costs [2].

Designed to overcome these limitations, the ER-SEE-P integrates advanced forward-viewing ultrasound technology, enabling real-time imaging of the papilla and improving guidewire placement accuracy. This approach reduces tissue trauma and enhances both procedural efficiency and safety [1].

Financially, the device addresses a substantial market opportunity. With over 600,000 annual ERCP procedures in the United States and a device price of $1,500, the serviceable addressable market (SAM) is estimated at $900 million. The total addressable market (TAM) for gastrointestinal endoscopic devices globally is approximately $30 billion [2]. These figures highlight the potential of the ER-SEE-P to meet unmet clinical needs while remaining commercially viable. Existing solutions rely on side-view duodenoscopes, which often fail to provide adequate visualization. By offering high-resolution imaging with a depth penetration of at least 1.5 cm, the ER-SEE-P enables gastroenterologists to perform procedures with greater precision while reducing complications. This innovation positions the device as a breakthrough in endoscopic technology, poised to significantly improve patient outcomes and procedural efficiency [2].

Design Research and Investigation Methodologies

The research phase for the ER-SEE-P device involved a comprehensive exploration of the clinical, technical, and procedural aspects of Endoscopic Retrograde Cholangiopancreatography (ERCP). This included an in-depth study of the procedure through literature reviews and instructional videos, which provided detailed insights into each step, such as guidewire placement and cannulation, and allowed for analysis of technique variations and physiological considerations. Additionally, devices currently used in ERCP were examined through the websites of leading companies, including Boston Scientific and Olympus. Specification sheets for relevant devices, such as intravascular ultrasound (IVUS) systems, were analyzed to understand the integration of small-scale ultrasound technology, informing the engineering parameters of the ER-SEE-P to ensure compatibility with existing workflows while incorporating forward-viewing ultrasound capabilities.

Interviews with gastroenterologists and fellows in the Atlanta area, including those from Emory University, were conducted to identify clinical needs and validate the device concept. These discussions highlighted challenges with current tools, particularly in visualizing the papilla, and associated risks such as pancreatitis and failed cannulation, underscoring the need for enhanced visualization tools.

A patent search was conducted using Google Scholar to identify prior art related to endoscopic and ultrasound-assisted devices. Relevant patents analyzed included US Patent 9380996B2, focusing on endoscopic imaging technologies, and US Patent 11992365B2, addressing endoscopic ultrasound applications. These patents were reviewed and deemed not to restrict the freedom to operate, confirming the novelty of the ER-SEE-P.

Guidance from the project's advisor, Dr. Sappati, further refined the conceptual framework of the ER-SEE-P. Dr. Sappati introduced the idea of forward-viewing ultrasound to improve visualization during ERCP, which became the foundation for the device, shaping its objectives to address critical clinical limitations. To refine the engineering design, an ultrasound researcher with expertise in guidewire imaging, Dr. Brooks Lindsey, provided recommendations for simulating imaging data using the Field II program, optimizing parameters such as imaging depth, resolution, and signal-to-noise ratios. Throughout the project, a multidisciplinary approach

was adopted, incorporating input from clinicians, biomedical engineers, and ultrasound researchers, ensuring that the final design was both technically feasible and clinically impactful.

Design Pivots and Updated Design Inputs Table

The initial design positioned the ultrasound probe inside the sphincterotome tip with a funnel to guide the wire. However, after receiving a sphincterotome from Dr. Sappati and noting the space occupied by the guidewire, the team revised the design to place the probe externally on the sphincterotome, eliminating the funnel and improving compatibility. As shown in Table 1, Dr. Sappati advised that the combined outer diameter of the sphincterotome and probe should not exceed the 4.2 mm inner diameter of the duodenoscope's working channel, rather than the previously assumed 2.3 mm [3]. Additionally, the probe length was constrained to the sphincterotome's 5 mm tip, with a ±1% tolerance [10].

Switching to an external probe required new functional considerations. Discussions with Dr. Brooks Lindsey confirmed that building a physical probe was unfeasible within the constraints, prompting a focus on simulating the transducer and defining performance parameters. The transducer needed a penetration depth of at least 1 cm, as specified by Dr. Sappati, with a center frequency of 5–20 MHz [5]. Imaging quality required a signal-to-noise ratio (SNR) above 50 dB and contrast-to-noise ratio (CNR) exceeding 30 dB [6, 14]. Axial and lateral resolutions were set at 1–2 mm to differentiate ducts from surrounding tissues [7], with beam widths below 0.3 mm and 2 mm for axial and lateral dimensions, respectively [8, 9].

These refinements ensured compatibility with existing ERCP tools and optimized visualization of bile and pancreatic ducts.

Table 1. Updated Design Inputs Table

Input Description	User Need(s)	Design Input (Engineering Term)	Metric	Citation
1. ENGINEERING				

A. Physical				
I. Dimensional Characteristics	Fit within existing duodenoscope channels	Maximum outer diameter	<4.2 mm	3
	Compatible with cannulation guidewire systems	Minimum inner diameter	≥2.67 Fr	4
	Probe must fit on tip of sphincterotome	Probe length	≤5.05 mm	10
II. Mechanical Characteristics	Must prevent trauma to tissues	Friction coefficient	≤0.04	11
	Sphincterotome maintains flexibility to navigate anatomy	Bending radius	15-25 mm	12
III. Functional Characteristics	Real-time ultrasound visualization of biliary and pancreatic ducts	Imaging depth	≥1.5 cm	13
		Peak energy depth	≥1 cm	Dr. Sappati
		Transducer center frequency	5-20 MHz	5
	Must acquire high-quality images	Signal-to-noise ratio	>50 dB	6
	Ducts are easy to distinguish from surrounding tissue	Contrast-to-noise ratio	>30 dB	14
		Axial beam width	<0.3 mm	8,9

	Ultrasound beam must be well-focused	Lateral beam width	<2 mm	8,9
	Must acquire high-resolution images	Axial resolution	1-2 mm	7
		Lateral resolution	1-2 mm	7
	Must allow guidewire insertion and retraction	% Resistance increase	<10%	4
	Must function in the patient's gastrointestinal tract	Internal body/gastrointestinal tract temperature	36-41 °C	15,16
IV. Electrical Characteristics	Electrical source (wall-powered or battery) for ultrasound device	Voltage	≥ 12V	17
	Must function for entire procedure	ERCP duration	≥200 minutes	18
B. Chemical / Biological	Material must be biocompatible	Material must not cause cytotoxicity, hypersensitivity, or irritation	Complies with Section 6.1 Paragraph 3 of ISO 10993-1	19
C. Environmental	Must work in the endoscopy suite	Temperature	20-23 °C	20
		Relative humidity	30-60%	20

D. Sterility / Sterilization	Must prevent infection	Sterile device using Ethylene Oxide (EtO) sterilization method	Ethylene oxide (EtO) product test of sterility (ToS) conducted to comply with ANSI/AAMI/ISO 11135:2014	[21], [22]
E. Packaging	Must ensure sterility until use	Hermetically sealed packaging with sterile indicators	Tamper-evident, sterile indicators	[22]
F. Reliability	Must reduce difficulty of accurate cannulation	Number of cannulation attempts	5 or fewer attempts	[23]
	Must reduce risk of post-ERCP pancreatitis	Cannulation time	<10.67 minutes	[23]
G. Storage / Shelf Life	The device must remain free from microbial growth for a sufficient time during which the device is stored prior to being used in a procedure	Contamination Rate	Colony-forming unit (CFU) Threshold	[24]

	Reduce frequency of reprocessing procedures	Single-use indication	Device IFU (Indications for Use)	24
2. HUMAN FACTORS/ ERGONOMICS	Must not introduce complexity in maneuverability	Total Weight	≤10-15 grams	Dr. Sappati
	No new training required to maneuver device	Additional Training Time	≤1 day	Dr. Sappati
3. LABELING	Clear instructions for use and sterility indicators	Sterile indicators and instructions for single use	Clear, legible labeling and inclusion of IFU	22

This table lists the final design specifications, with critical inputs highlighted in yellow and updates from the original Design Inputs Report shown in red font, reflecting refinements for functionality and compatibility.

Proposed Design

This design prioritizes usability by integrating seamlessly with existing devices. The compact transducer (1.5 mm width, 5 mm length) fits the sphincterotome without obstructing maneuverability or cutting wire functionality. It slides smoothly through standard working channels (4.2–4.8 mm) at a maximum diameter of 3.6 mm, as shown in Figure 2 [25]. The 1.5 cm focus depth aligns with the maximum distance from the sphincterotome tip to duct divergence, improving cannulation accuracy and minimizing patient injury risk [26].
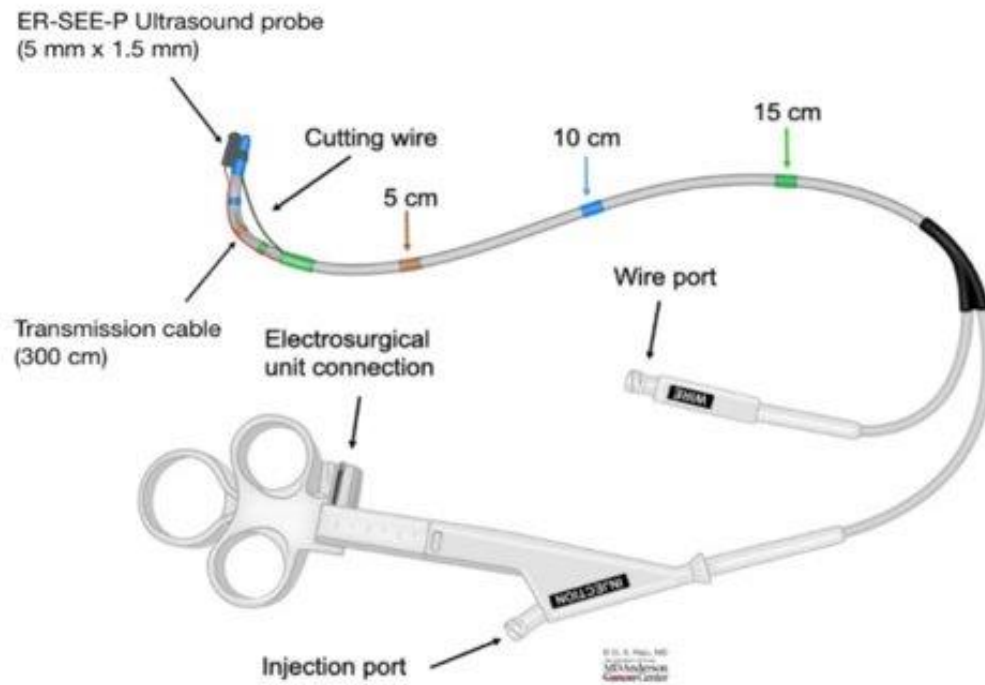

Figure 2. ER-SEE- device fitted onto a Boston scientific sphincterotome, to scale.

Optimization of the ultrasound system used MATLAB-based Field II software, which applies the Rayleigh-Sommerfeld diffraction integral to predict acoustic fields. Using spatial impulse responses, it calculates transducer pressure fields in a homogeneous medium [27]. Field II's beam profiles and pulse-echo simulations, validated against experimental data, provide key

insights into image formation and signal behavior [28]. The full simulation code is in Appendix III.

Frequencies within the range of 8–12 MHz are commonly utilized in diagnostic imaging for superficial and mid-depth structures [5]. The selected center frequency (f_0) of 10 MHz provides an optimal balance between sufficient depth penetration (1–1.5 cm) and high resolution.

The sampling frequency (f_s) of 100 MHz is ten times the center frequency. This oversampling exceeds the Nyquist criterion, ensuring accurate digitization of acoustic signals [29, 30].

A simulated speed of sound (c) of 1540 m/s, a standard value for soft tissues, ensured accurate modeling of wave propagation, depth calibration, consistent phase alignment, and focal zone accuracy [31].

Introducing a matching layer minimized acoustic impedance mismatch, improved energy transmission between the piezoelectric elements and tissue, and improved image clarity [32]. Based on the quarter-wavelength principle, a matching layer thickness of 0.02 mm ensured constructive interference and optimal energy transfer [33]. The material's speed of sound at 2000 m/s was optimal for maintaining compatibility between the piezoelectric elements and soft tissue [34].

A sinusoidal signal matching the 10 MHz center frequency generated a basic impulse response. The calculated delay introduced by the matching layer—based on its thickness and the speed of sound—was incorporated into the simulation by prepending zero values to the impulse response array [35]. A Hann window smoothed the edges of the impulse and reduced spectral artifacts [36].

The excitation signal represents the electrical input applied to the transducer's piezoelectric elements. A sinusoidal signal with a frequency of 10 MHz and an amplitude amplified by a factor of 30 ensured sufficient acoustic energy for imaging at the 15 mm focal depth. Limiting the signal to two cycles balanced spatial resolution with adequate energy generation [37].

Apodization modifies the amplitude of the excitation signal across the transducer elements to suppress side lobes that introduce imaging artifacts and degrade contrast. A Chebyshev window

with a -30 dB side lobe suppression level minimized energy loss outside the main beam while preserving the beam's focus [38].

Selecting the optimal array type for the ultrasound transducer was critical to achieving the desired beam focus, resolution, field of view, and compatibility with the forward-viewing probe [39]. Simulations compared linear, phased, and curved linear arrays. Linear arrays, though effective for shallow, uniform imaging, lacked the depth penetration and focus required for curved and confined regions like the ampulla of Vater and ducts, and their planar geometry was incompatible with the sphincterotome's forward-viewing design. Phased arrays offered deep imaging and beam steering but suffered from poor lateral resolution at shallow depths, limiting their ability to resolve fine features like ductal openings. The curved linear array emerged as the optimal configuration, with its convex element arrangement aligning naturally with the duodenal anatomy, providing a wider field of view, enhanced beam focus, and consistent lateral and axial resolution across the imaging plane [39].

Once the curved linear array was selected, iterative testing refined the radius of curvature. Smaller radii (<15 mm) improved shallow-depth resolution but narrowed the field of view. Larger radii (>25 mm) enhanced depth penetration but reduced resolution [40]. A 20 mm radius was determined to strike the ideal balance.

The kerf, or spacing between transducer elements, was set to 6 μm to optimize spatial resolution within the transducer's compact dimensions. This size suppresses grating and side lobes, while still being feasible for manufacturing [41]. At the 10 MHz center frequency, the wavelength (λ) was calculated as 154 μm using the formula $\lambda = \frac{c}{f_0}$, where c is 1540 m/s. The element width needed to be less than half the wavelength ($\frac{\lambda}{2}$), resulting in an initial width of approximately 77 μm, which ensures effective wave propagation, minimal side lobes, and improved lateral resolution [42]. This final element width was 0.051923 mm, with calculations further explained in the Engineering Analyses, leading to a final design with 26 elements, as seen in Figure 3.
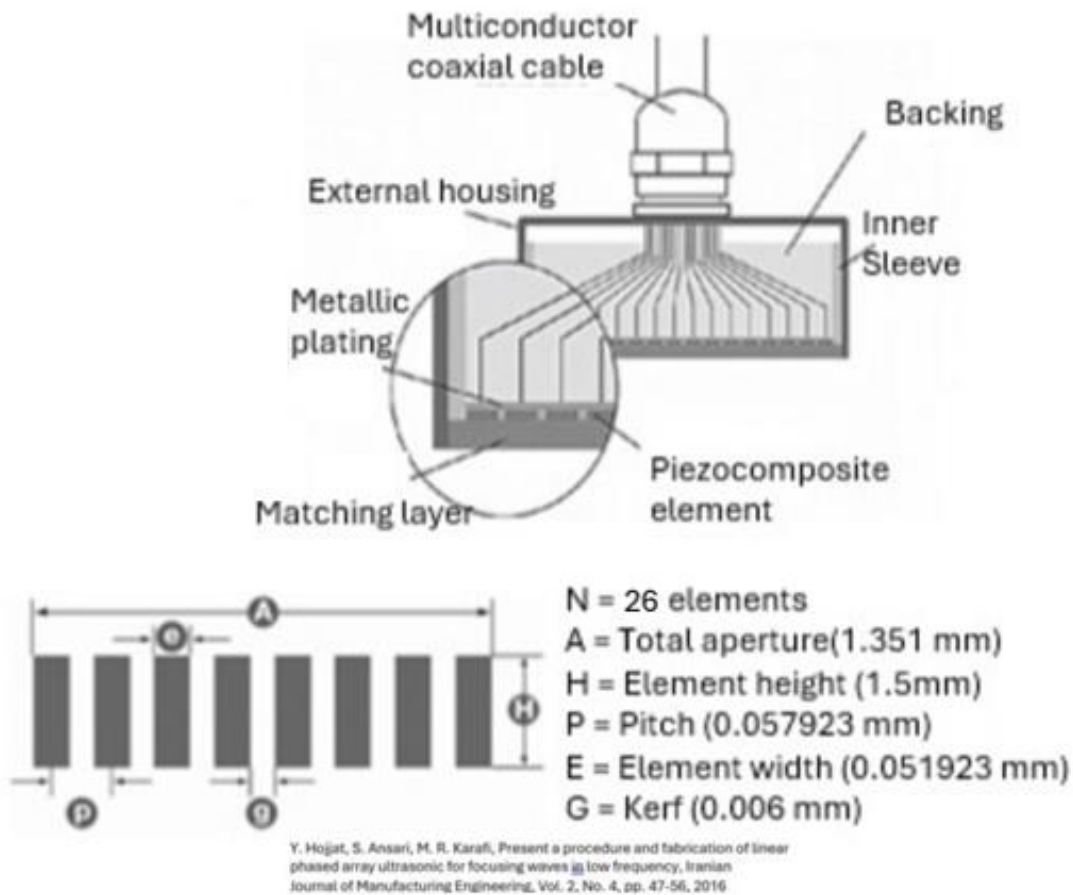
Figure 3. Schematic of array components and dimensions for the ER-SEE-P.

The proposed transducer utilizes high-performance materials used in similar ultrasound systems. The array of efficient and durable piezoelectric elements made from lead zirconate titanate (PZT) costs approximately $200 [43]. The matching layer, constructed from an epoxy-resin composite with a speed of sound of 2000 m/s, costs around $50 [44]. Tungsten-filled epoxy backing material, priced at $80, ensures effective damping [45]. The housing uses biocompatible polyurethane, with an estimated cost of $30 [46]. Micro-coaxial cables for compact signal transmission, add about $20 to the total [47].
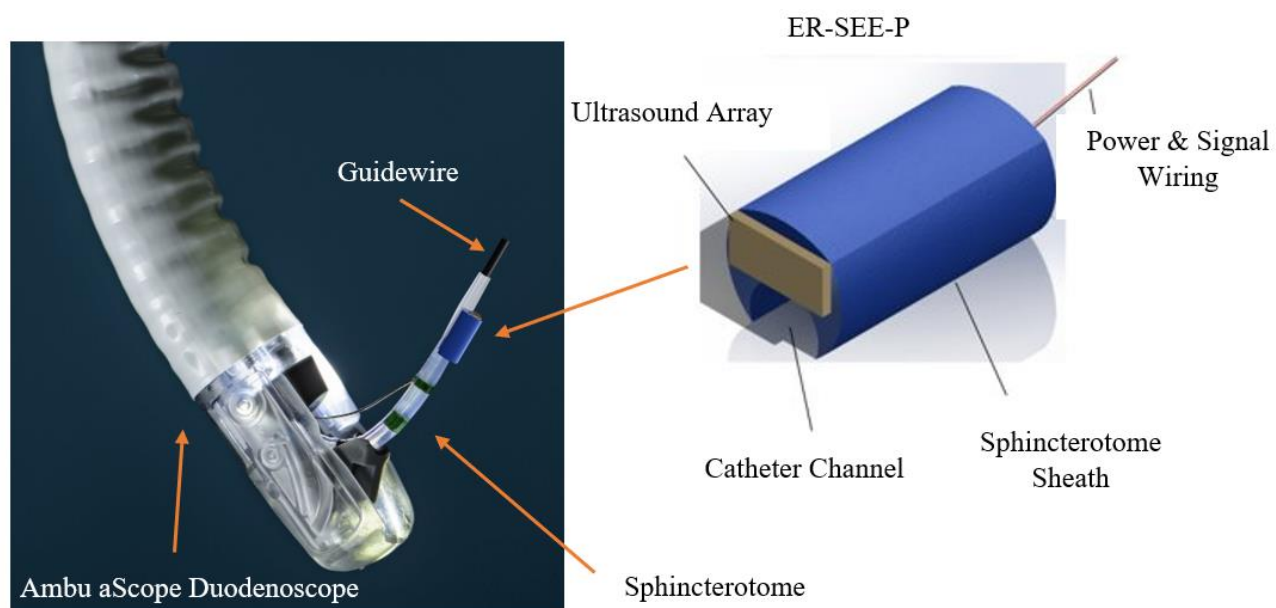
Prototype

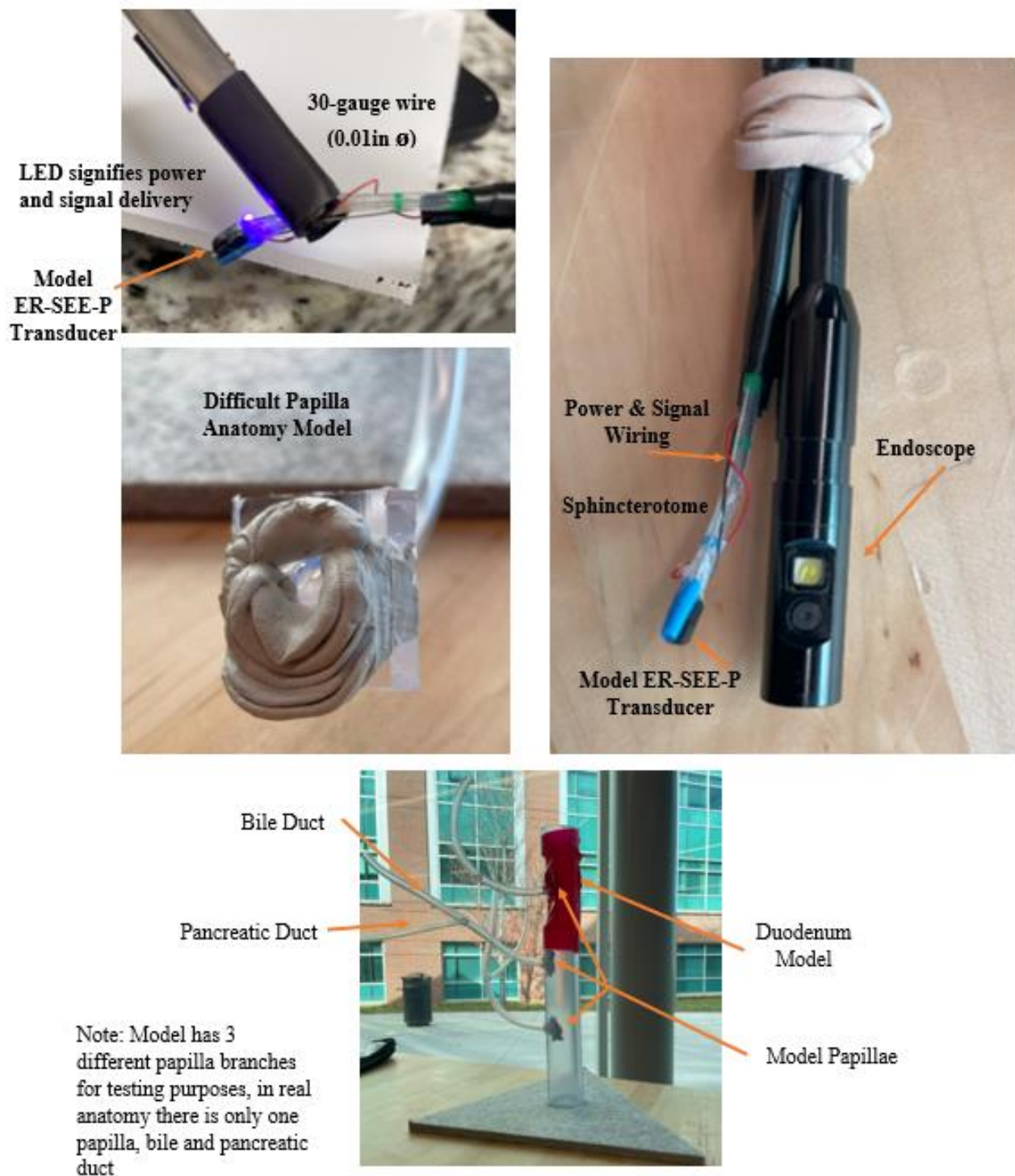Figure 4. CAD rendering of ER-SEE-P attached to a duodenoscope 48

Figure 5. Physical Prototype and Testing Materials including the ER-SEE-P with an LED (top left), the ER-SEE-P with an Endoscope (top right), a Difficult Papilla Anatomy Model (middle left), and a Duodenum Testing Model (bottom)

Engineering Analysis

The length of the transducer was verified to be 5.01 mm (Figure 6), less than the maximum value of 5.05 mm. Therefore, the transducer length does not extend farther than the non-bending portion of the sphincterotome.

Figure 6. Verification of ER-SEE-P Length

The diameter of the transducer attached to the sphincterotome was verified to be 3.58 mm (Figure 7). This is well within the maximum diameter of all standard ERCP duodenoscope working channels, which range from 4.2 to 4.8mm[49].

Figure 7. Verification of Overall Outer Diameter of ER-SEE-P Probe and Sphincterotome

An LED with 30-gauge wire (0.01in) was attached along the length of the sphincterotome and successfully switched on and off (Figure 8). This supports that the target of 18–24-gauge wire

(0.04-0.02 in), larger sized wires and cables, would be feasible to use in a working ultrasound of this size.

Figure 8. LED with 30-Gauge Wire Verification Test

Validation testing of 6 different papillae anatomies that modeled those of Figure 9 [50] was performed to validate that the device could still maneuver and perform the desired procedure with the ER-SEE-P transducer attached. The device successfully passed all testing requirements and an example video in Appendix II provides a thorough overview of that process.

PAPILLA MORPHOLOGY	Type 1 (Regular)	Type 2 (Small)	Type 3 (Protruding)	Type 4 (Creased/Ridged)
Prevalence	56%	13%	23%	8%
Cannulation Failure	2% (REF)	12% (OR 7.9)*	11% (OR 7.3) *	6% (OR 3.9)
Difficult Cannulation	36%	52%*	48%*	43%
Pancreatitis	7%	20%*	2%	6%

Figure 9. Papilla Morphology [51]

To evaluate the ER-SEE-P's performance in Field II, a phantom was created to simulate anatomical structures, including the ampulla of Vater, duodenal papilla, biliary duct, and pancreatic duct, using scatterers to replicate spatial positioning, size, and reflectivity.

Field II simulations iteratively optimized the transducer's element count for beam steering, dynamic focusing, reduced beam divergence, grating lobe suppression, and improved spatial resolution [52]. Starting with a 77 μm element width, the number of elements was increased until reaching the smallest manufacturable width of 0.051923 mm, resulting in 26 elements within the 1.5 mm transducer [53].

The phantom modeled acoustic properties: the ampulla of Vater at 15 mm depth with high reflectivity (0.9–1.0), the biliary duct at 16 mm with a 4 mm diameter and reflectivity of 0.75–0.8, and the pancreatic duct at 17 mm with a 2–3 mm diameter and reflectivity of 0.8–0.85 [26].

Simulations propagated acoustic waves into the phantom, capturing reflected signals to extract maximum intensity values across lateral and depth positions. These generated a beam profile matrix used to analyze acoustic energy distribution, resolution, and feature distinction [54].
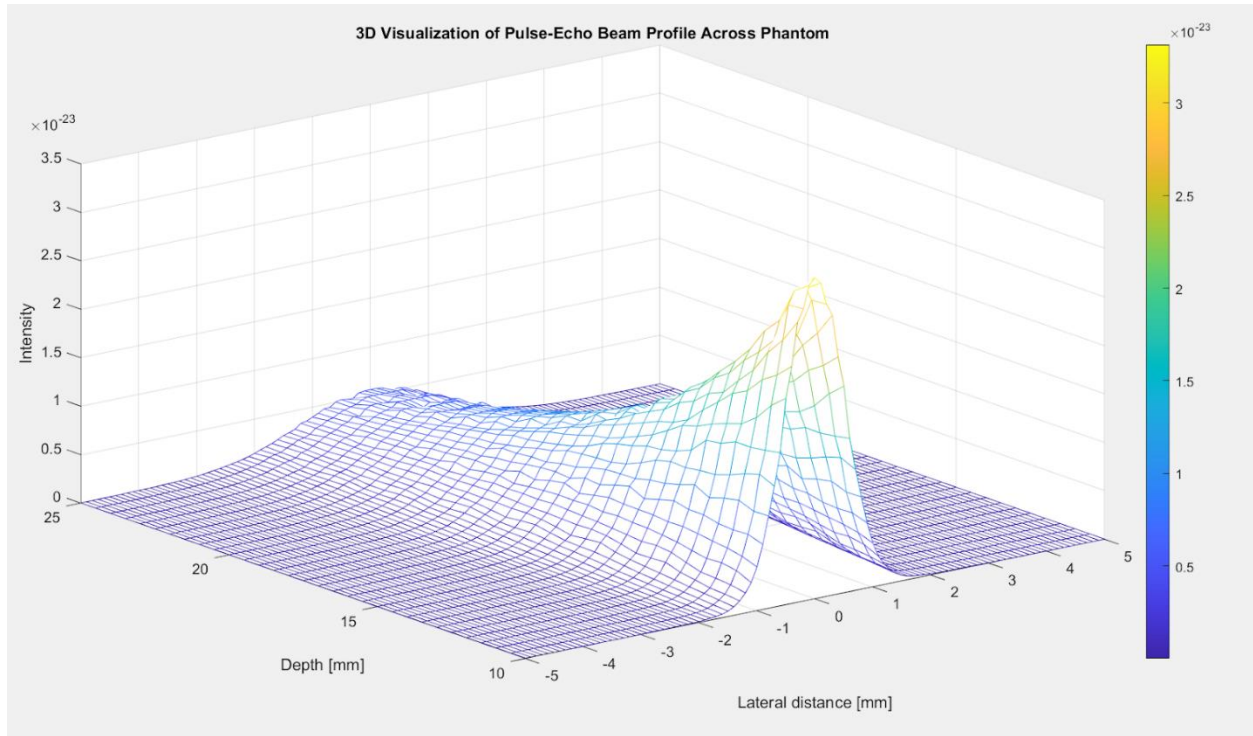
Figure 10. 3D visualization of the beam profile across a tissue-mimicking phantom, demonstrating focused energy distribution at the target depth.

The 3D visualization of the beam profile, shown in Figure 10, illustrates the acoustic intensity distribution across lateral and depth dimensions in the simulated phantom [54]. It highlights the transducer's focused ultrasound energy interacting with the modeled anatomical structures. The energy is concentrated at a depth of 10–15 mm, corresponding to the focal depth. The lateral dimension displays beam spread and alignment with anatomical targets, while the depth axis shows the gradual attenuation of intensity as the waves penetrate the phantom. Bright regions near the focus indicate high-intensity zones, while the attenuation away from the focal point demonstrates the natural decay of ultrasound waves.
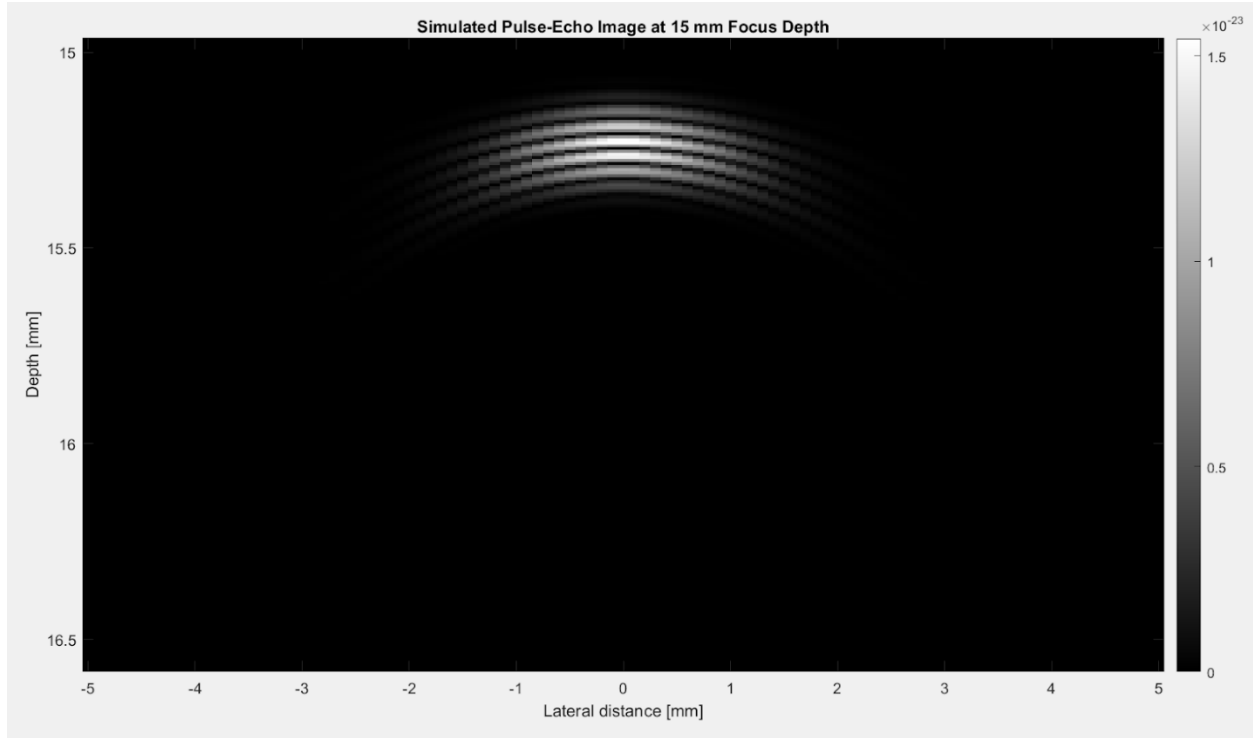
Figure 11. Reconstructed pulse-echo image at the focal depth of 15 mm, highlighting the transducer's ability to resolve critical anatomical structures with clarity.

Figure 11, a 2D grayscale pulse-echo image, provides a focused representation of the reconstructed ultrasound output at the transducer's focal depth. The intensity variations captured in the grayscale reflect the acoustic reflections from the phantom's scatterers, illustrating the system's ability to resolve anatomical structures with clarity and precision. The image serves as a complementary analysis to the 3D beam profile, offering a closer and more detailed examination of the transducer's performance at the focal plane to demonstrate the quality of imaging resolution and the degree of distortion [54]. The distinct intensity bands in the image verify the transducer's capacity to differentiate closely spaced structures.

The performance of an ultrasound transducer was further assessed through key parameters that directly impact image quality and diagnostic reliability [55]These parameters included signal-to-noise ratio (SNR), contrast-to-noise ratio (CNR), lateral and axial beamwidth at the -6 dB level, peak energy depth, and lateral and axial resolution derived from the Point Spread Function (PSF).

To calculate SNR, a region of the beam profile corresponding to the main signal was selected as the signal region. The mean intensity ($mean_{signal}$) and standard deviation (std_{signal}) within this region were computed. Noise was measured from the peripheral areas of the beam profile and its standard deviation (std_{noise}) was calculated. SNR was then determined using the formula: $SNR(dB) = 20 \cdot \log_{10} \left(\frac{mean_{signal}}{std_{noise}} \right)$. In this design, the calculated SNR was 55.261 dB, indicating strong signal clarity and surpassing the clinical threshold of 50 dB required for high-quality imaging [6].

To calculate CNR, a secondary region of interest, defined as the contrast region, was selected to represent an area with a different intensity from the primary signal region. The mean intensity of the contrast region ($mean_{constrast}$) was determined, and the absolute difference between the signal and contrast means was used to quantify contrast. This value was then normalized by the noise standard deviation and converted to decibels: $CNR(dB) = 20 \cdot \log_{10} \left(\frac{|mean_{signal} - mean_{contrast}|}{std_{noise}} \right)$. The calculated CNR was 38.74 dB, demonstrating the transducer's ability to differentiate between closely spaced or acoustically similar structures and surpassing the clinical threshold of 30 dB required for high-quality imaging [14].

Lateral and axial beam widths were measured at the -6 dB intensity level, corresponding to half the maximum intensity [9]. The analysis identified the beam profile's maximum intensity value (max_value) and its location, establishing the reference point for the -6 dB level, mathematically defined as half the peak amplitude. This standard ensures consistent quantification of beam dimensions relative to the region of highest intensity ($-6\ dB\ level = \frac{max\_value}{\sqrt{2}}$). The lateral beam profile, depicting intensity distribution across the beam width at the depth of maximum intensity, was analyzed to determine the lateral beam width. Points where the lateral intensity met or exceeded the -6 dB threshold were identified, and the distance between these positions was calculated [9]. This distance was converted into millimeters using the simulation's spatial resolution, yielding a lateral beam width of 1 mm. This sharp focus is essential for distinguishing closely spaced anatomical features in the imaging plane. Similarly, the axial beam profile, representing intensity distribution along the depth axis, was analyzed, resulting in an axial beam

width of 0.0847 mm. This demonstrates excellent resolution along the beam propagation axis, critical for precise imaging of anatomical structures [8].

Peak energy depth analysis summed beam intensity values laterally across all positions at each depth within the simulated beam profile, generating a depth energy distribution. The peak depth, corresponding to the beam's most focused portion, was found at 1 cm [26], ensuring optimal image clarity and meeting the critical design metric for visualizing anatomical structures like the ampulla of Vater and ducts during ERCP.

Point spread function (PSF) analysis evaluated the transducer's beam sharpness and spatial resolution using a single point scatterer [54]. At a focal depth of 15 mm, lateral and axial scan points extended 5 mm around the scatterer to capture the spatial profile. Pulse-echo simulations produced a 2D intensity matrix, and -6 dB thresholds determined lateral and axial resolutions. Both resolutions were 2 mm, confirming the transducer's ability to produce a sharply focused, high-resolution beam [7].
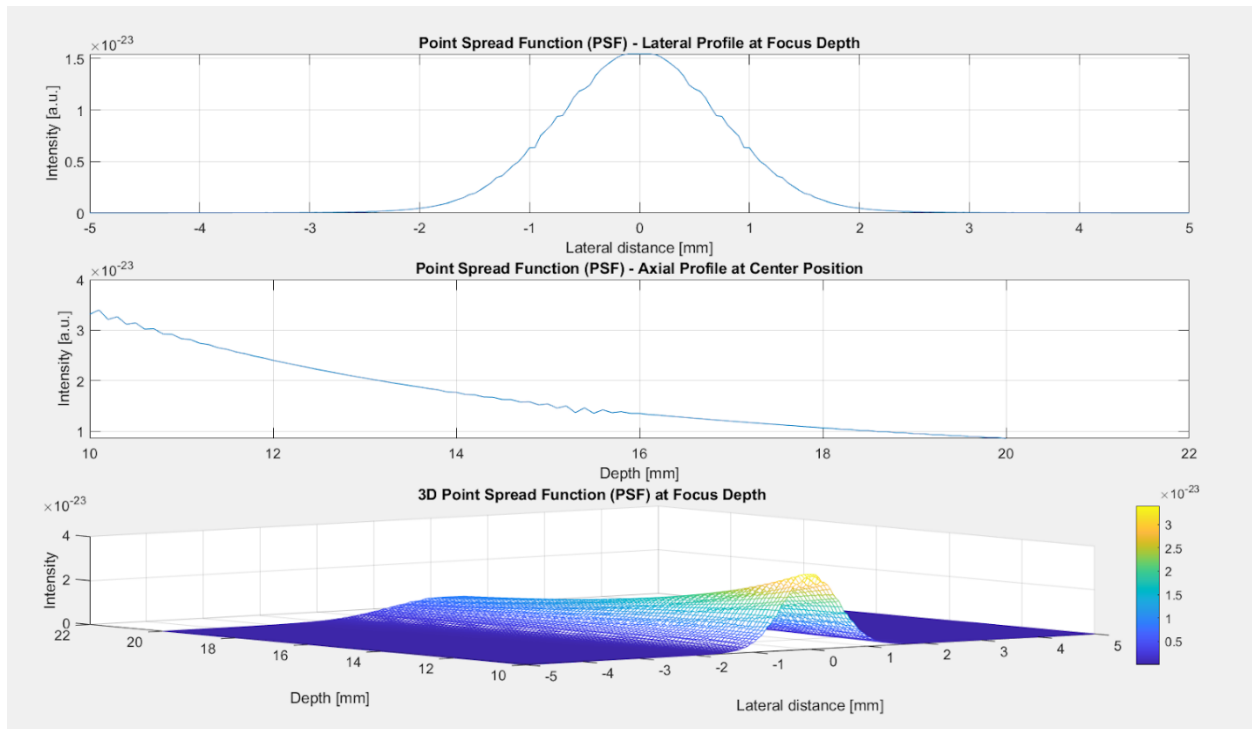

Figure 12. Point spread function analysis of a single scatterer at 15 mm, quantifying lateral and axial resolutions at the -6 dB intensity threshold.

Figure 12 provides a comprehensive analysis of the point spread function (PSF) at the 15 mm focal depth. The first panel shows the lateral PSF profile, with a symmetric curve and steep fall-off around the center, indicating optimized lateral resolution for distinguishing adjacent features in clinical imaging [54]. The second panel displays the axial PSF profile along the depth axis, centered at the same lateral position. The tapering intensity away from the focal point confirms a well-defined focus at the target depth, minimizing signal spillover to adjacent depths. The third panel combines lateral and axial dimensions into a 3D visualization of the PSF. The uniform peak highlights the transducer's capability for high-resolution imaging with minimal distortion.

Future Work

The next phase for the ultrasound transducer involves transitioning from simulations to manufacturing and performance validation. Achieving the compact specifications requires precision techniques such as deep reactive ion etching (DRIE) for precise element spacing with kerfs as narrow as 6 μm [41]. The matching layer will use silver epoxy for optimal acoustic impedance, minimizing reflection losses and enhancing energy transmission [56]. Assembly techniques like flexible printed circuits (FPCs) and conductive epoxy soldering will ensure compact, reliable electrical connections with minimal interference [41]. Proper alignment of piezoelectric elements, the backing layer, and the matching layer is essential for efficient energy delivery and high-performance imaging [56].

Physical pulse-echo and spatial resolution testing will validate simulated performance while accounting for material inconsistencies and manufacturing tolerances [41][56]. Testing will use tissue-mimicking phantoms replicating the ampulla of Vater and surrounding ducts to assess metrics such as lateral and axial resolutions, signal-to-noise ratio (SNR), and contrast-to-noise ratio (CNR), comparing results to simulation benchmarks for optimal imaging clarity. Clinical evaluation will follow a stepwise approach: starting with phantoms, progressing to cadaveric models, and eventually animal studies to validate usability and imaging accuracy during ERCP [41]. Key metrics, such as resolution maintenance during anatomical movement, will inform refinements. Transitioning to human trials under IRB approval will be essential for regulatory submissions, with FDA approval requiring evidence of safety, efficacy, and usability through trials with experienced endoscopists.

Securing funding will be crucial to advance prototyping, manufacturing, and clinical testing. Potential sources include NIH or NSF research grants and collaborations with medical imaging companies to provide financial and technical resources.

References

1. Chandrasekhara V, Khashab MA, Muthusamy VR, et al. Adverse events associated with ERCP. *Gastrointestinal Endoscopy*. 2017;85(1):32-47. doi:https://doi.org/10.1016/j.gie.2016.06.051

2. Adler DG. Top 10 things to remember when cannulating the bile duct in patients with native papillary anatomy during ERCP (with videos). *Gastrointestinal Endoscopy*. 2021;94(5):995-997. doi:https://doi.org/10.1016/j.gie.2021.08.001

3. Ang TL, Seewald S, Nib Soehendra. Stent Removal: Migrated and Non-Migrated. *Elsevier eBooks*. Published online January 1, 2008:177-187. doi:https://doi.org/10.1016/b978-1-4160-4271-6.50023-x

4. Singhvi G, Dea SK. Guidewires in ERCP. *Gastrointestinal Endoscopy*. 2013;77(6):938-940. doi:https://doi.org/10.1016/j.gie.2012.12.016

5. Grogan SP, Mount CA. Ultrasound Physics and Instrumentation. Nih.gov. Published 2021. https://www.ncbi.nlm.nih.gov/books/NBK570593/

6. Zahra Mardi, Mahloojifar A. Signal to Noise Ratio Improvement of Ultrasound Harmonic Images Using Coded Excitation and Adaptive Line Enhancer. Published online May 1, 2018. doi:https://doi.org/10.1109/icee.2018.8472442

7. Chen C, Hendrik, Hendriks M, Menssen J, Lu JY, Chris. Point Spread Function Formation in Plane-Wave Imaging: A Theoretical Approximation in Fourier Migration. *IEEE Transactions on Ultrasonics Ferroelectrics and Frequency Control*. 2019;67(2):296-307. doi:https://doi.org/10.1109/tuffc.2019.2944191

8. Scholten HJ, Weijers G, de Wild M, Korsten HHM, de Korte CL, Bouwman RA. Differences in ultrasound elevational beam width (slice thickness) between popular handheld devices. *WFUMB Ultrasound Open*. 2023;1(2):100009. doi:https://doi.org/10.1016/j.wfumbo.2023.100009

9. Thijssen JM, Weijers G, de Korte CL. Objective Performance Testing and Quality Assurance of Medical Ultrasound Equipment. *Ultrasound in Medicine & Biology*. 2007;33(3):460-471. doi:https://doi.org/10.1016/j.ultrasmedbio.2006.09.006

10. Dreamtome™ RX Cannulating Sphincterotome. www.bostonscientific.com. Published 2024. https://www.bostonscientific.com/en-US/products/sphincterotomes/dreamtome-rx-cannulating-sphincterotome.html

11. Walker JS. *Solutions Manual for Students to Accompany Physics for Scientists and Engineers, Third Edition, by Paul A. Tipler*. W H Freeman & Company; 1991.

12. Köksal AŞ, Eminler AT, Parlak E. Biliary endoscopic sphincterotomy: Techniques and complications. *World Journal of Clinical Cases*. 2018;6(16):1073-1086. doi:https://doi.org/10.12998/wjcc.v6.i16.1073

13. Anatomy of the Liver & Gallbladder | SEER Training. training.seer.cancer.gov. https://training.seer.cancer.gov/biliary/anatomy/liver.html

14. Rodriguez-Molares A, Rindal OMH, D'hooge J, et al. The Generalized Contrast-to-Noise Ratio: A Formal Definition for Lesion Detectability. *IEEE Transactions on Ultrasonics, Ferroelectrics, and Frequency Control*. 2020;67(4):745-759. doi:https://doi.org/10.1109/tuffc.2019.2956855

15. Hepburn JS, Eberhard HM, Ricketts R, Rieger CLW. TEMPERATURE OF THE GASTROINTESTINAL TRACT: THE EFFECT THEREON OF HOT AND COLD FOODS AND OF PHYSICAL THERAPEUTIC AGENTS. *Archives of Internal Medicine*. 1933;52(4):603-615. doi:https://doi.org/10.1001/archinte.1933.00160040109006

16. Hosokawa Y, Adams WM, Stearns RL, Casa DJ. Comparison of Gastrointestinal and Rectal Temperatures During Recovery After a Warm-Weather Road Race. *Journal of Athletic Training*. 2016;51(5):382-388. doi:https://doi.org/10.4085/1062-6050-51.7.02

17. Electronic Products, Electronic Products. Powering medical ultrasound imaging - Electronic Products. Electronic Products. Published July 31, 2012. Accessed December 9, 2024. https://www.electronicproducts.com/powering-medical-ultrasound-imaging

18. Mehta PP, Sanaka MR, Parsi MA, et al. Association of procedure length on outcomes and adverse events of endoscopic retrograde cholangiopancreatography. 2014;2(2):140-144. doi:https://doi.org/10.1093/gastro/gou009

19. ISO-10993-1:2009. October 15, 2009. Accessed September 16, 2024. https://nhiso.com/wp-content/uploads/2018/05/ISO-10993-1-2009.pdf.

20. Endoscopy Suite Architectural Design. Accessed September 23, 2024. https://www.cdc.gov/niosh/docket/archive/pdfs/NIOSH-159/0159-020109-Sheet406.pdf.

21. Muscarella LF. New Guidance for Hospitals Considering the Sterilization of Flexible Endoscopes - Discussions in Infection Control. Discussions in Infection Control. Published May

30, 2019. Accessed December 9, 2024. https://lfm-hcs.com/2019/05/new-guidance-for-hospitals-considering-the-sterilization-of-flexible-endoscopes/

22. 14:00-17:00. ISO 11607-2:2019. ISO. https://www.iso.org/standard/70800.html

23. Meseeha M, Attia M. Endoscopic Retrograde Cholangiopancreatography (ERCP). PubMed. Published 2020. https://www.ncbi.nlm.nih.gov/books/NBK493160/

24. Harishankar Gopakumar, Vohra I, Sharma NR, Puli SR. Performance of single-use duodenoscopes for ERCP: a systematic review and meta-analysis. *iGIE*. 2022;1(1):77-84. doi:https://doi.org/10.1016/j.igie.2022.10.014

25. Varadarajulu S, Banerjee S, Barth BA, et al. GI endoscopes. *Gastrointestinal Endoscopy*. 2011;74(1):1-6.e6. doi:https://doi.org/10.1016/j.gie.2011.01.061

26. Tae Un Kim, Kim S, Jun Woo Lee, et al. Ampulla of Vater: Comprehensive anatomy, MR imaging of pathologic conditions, and correlation with endoscopy. *European journal of radiology*. 2008;66(1):48-64. doi:https://doi.org/10.1016/j.ejrad.2007.04.005

27. Jensen JA. Simulation of advanced ultrasound systems using Field II. *2004 2nd IEEE International Symposium on Biomedical Imaging: Macro to Nano (IEEE Cat No 04EX821)*. doi:https://doi.org/10.1109/isbi.2004.1398618

28. Gao H, Hergum T, Torp H, D'hooge J. Comparison of the performance of different tools for fast simulation of ultrasound data. *Ultrasonics*. 2012;52(5):573-577. doi:https://doi.org/10.1016/j.ultras.2012.01.009

29. Botz B. Nyquist limit. *Radiopaediaorg*. Published online August 21, 2020. doi:https://doi.org/10.53347/rid-81286

30. Kirchhof J, Semper S, Wagner CW, Pérez E, Römer F, Galdo D. Frequency Sub-Sampling of Ultrasound Non-Destructive Measurements: Acquisition, Reconstruction and Performance. *arXiv (Cornell University)*. Published online January 1, 2020. doi:https://doi.org/10.48550/arxiv.2012.04534

31. Shin HC, Prager R, Gomersall H, Kingsbury N, Treece G, Gee A. Estimation of Average Speed of Sound Using Deconvolution of Medical Ultrasound Data. *Ultrasound in Medicine & Biology*. 2010;36(4):623-636. doi:https://doi.org/10.1016/j.ultrasmedbio.2010.01.011

32. Rathod VT. A Review of Acoustic Impedance Matching Techniques for Piezoelectric Sensors and Transducers. *Sensors*. 2020;20(14):4051. doi:https://doi.org/10.3390/s20144051

33. Wang T, Chen G, Zhu J, Gong H, Zhang L, Wu H. Deep understanding of impedance matching and quarter wavelength theory in electromagnetic wave absorption. *Journal of Colloid and Interface Science*. 2021;595:1-5. doi:https://doi.org/10.1016/j.jcis.2021.03.132

34. Lee T, Jung J, Lee SM, et al. FPCB as an Acoustic Matching Layer for 1D Linear Ultrasound Transducer Arrays. *Sensors (Basel)*. 2022;22(15):5557-5557. doi:https://doi.org/10.3390/s22155557

35. Gehrke T, F. Cheikhrouhou, Overhoff HM. Derivation of the impulse response of ultrasonic transducers by experimental system identification. 2006;1:349-352. doi:https://doi.org/10.1109/ultsym.2005.1602866

36. Stromer J, Ladani L. Examination of a spectral-based ultrasonic analysis method for materials characterization and evaluation. *Biomedical Signal Processing and Control*. 2018;40:454-461. doi:https://doi.org/10.1016/j.bspc.2017.10.010

37. Weng C, Gu X, Jin H. Coded Excitation for Ultrasonic Testing: A Review. *Sensors*. 2024;24(7):2167-2167. doi:https://doi.org/10.3390/s24072167

38. Wang P, Liang J, Li X. Depth-dependent apodization window based on Chebyshev polynomial for ultrasound imaging. *The Journal of the Acoustical Society of America*. 2022;152(1):19-30. doi:https://doi.org/10.1121/10.0011917

39. Drinkwater BW, Wilcox PD. Ultrasonic arrays for non-destructive evaluation: A review. *NDT & E international*. 2006;39(7):525-541. doi:https://doi.org/10.1016/j.ndteint.2006.03.006

40. Elloian J, Jakub Jadwiszczak, Arslan V, Sherman JD, Kessler D, Shepard KL. Flexible ultrasound transceiver array for non-invasive surface-conformable imaging enabled by geometric phase correction. *Scientific Reports*. 2022;12(1). doi:https://doi.org/10.1038/s41598-022-20721-7

41. Cabrera-Munoz NE, Eliahoo P, Wodnicki R, et al. Forward-looking 30-MHz phased-array transducer for peripheral intravascular imaging. *Sensors and Actuators A: Physical*. 2018;280:145-163. doi:https://doi.org/10.1016/j.sna.2018.07.035

42. Yoon H, Song TK. Sparse Rectangular and Spiral Array Designs for 3D Medical Ultrasound Imaging. *Sensors*. 2019;20(1):173. doi:https://doi.org/10.3390/s20010173

43. Lu H, Cui H, Lu G, et al. 3D Printing and processing of miniaturized transducers with near-pristine piezoelectric ceramics for localized cavitation. *Nature communications*. 2023;14(1). doi:https://doi.org/10.1038/s41467-023-37335-w

44. Fang HJ, Chen Y, Wong CM, et al. Anodic aluminum oxide–epoxy composite acoustic matching layers for ultrasonic transducer application. *Ultrasonics*. 2016;70:29-33. doi:https://doi.org/10.1016/j.ultras.2016.04.003

45. Hidayat D, Setianto Setianto. Control of tungsten-epoxy composite porosity prepared using a high-energy ball milling method: an engineering aspect of backing layer fabrication. *Journal of Science Advanced Materials and Devices*. Published online September 1, 2024:100793-100793. doi:https://doi.org/10.1016/j.jsamd.2024.100793

46. Marois Y, Guidoin R. *Biocompatibility of Polyurethanes*. Landes Bioscience; 2013. https://www.ncbi.nlm.nih.gov/books/NBK6422/

47. He Y, Liu X, Zhang J, Peng C. A Backing-Layer-Shared Miniature Dual-Frequency Ultrasound Probe for Intravascular Ultrasound Imaging: In Vitro and Ex Vivo Validations. *Biosensors*. 2023;13(11):971. doi:https://doi.org/10.3390/bios13110971

48. ENG. Ambu aScope Duodeno - ENG. Ambu-external. Published 2020. https://video.ambu.com/ambu-ascope-duodeno-eng

49. Bang JY, Hawes R, Varadarajulu S. Equivalent performance of single-use and reusable duodenoscopes in a randomised trial. *Gut*. Published online September 7, 2020:gutjnl-2020-321836. doi:https://doi.org/10.1136/gutjnl-2020-321836

50. Mohamed R, Lethebe BC, Gonzalez-Moreno E, et al. Morphology of the major papilla predicts ERCP procedural outcomes and adverse events. *Surgical Endoscopy*. 2020;35(12):6455-6465. doi:https://doi.org/10.1007/s00464-020-08136-9

51. Cahyadi O, Tehami N, de-Madaria E, Siau K. Post-ERCP Pancreatitis: Prevention, Diagnosis and Management. *Medicina*. 2022;58(9):1261. doi:https://doi.org/10.3390/medicina58091261

52. Long J, Long W, Bottenus N, Trahey G. Coherence-based quantification of acoustic clutter sources in medical ultrasound. *The Journal of the Acoustical Society of America*. 2020;148(2):1051-1062. doi:https://doi.org/10.1121/10.0001790

53. Cummins T, Eliahoo P, Kirk Shung K. High-Frequency Ultrasound Array Designed for Ultrasound-Guided Breast Biopsy. *IEEE Transactions on Ultrasonics, Ferroelectrics, and Frequency Control*. 2016;63(6):817-827. doi:https://doi.org/10.1109/tuffc.2016.2548993

54. Jensen J, Svendsen NB. Calculation of pressure fields from arbitrarily shaped, apodized, and excited ultrasound transducers. *IEEE Transactions on Ultrasonics Ferroelectrics and Frequency Control*. 1992;39(2):262-267. doi:https://doi.org/10.1109/58.139123

55. Peralta L, Ramalli A, Reinwald M, Eckersley RJ, Hajnal JV. Impact of Aperture, Depth, and Acoustic Clutter on the Performance of Coherent Multi-Transducer Ultrasound Imaging. *Applied Sciences*. 2020;10(21):7655. doi:https://doi.org/10.3390/app10217655

56. Peng J, Peng X, Tang H, et al. Fabrication and Performance of a Miniaturized and Integrated Endoscope Ultrasound Convex Array for Digestive Tract Imaging. *IEEE Transactions on Biomedical Engineering*. 2018;65(1):140-148. doi:https://doi.org/10.1109/tbme.2017.2696560

Appendix

I. Expo Poster

EXPO Poster.pptx

II. Demonstration Video

ER-SEE-P Normal Anatomy

III. Ultrasound Simulation Code

```matlab
 % Step 1: Define Transducer Parameters - Field II-Specific
% Initialize Field II and display configuration info
field_init; % Initialize Field II toolbox
field_info; % Display Field II configuration
% Define parameters
f0 = 10e6; % Center frequency in Hz (10 MHz)
fs = 100e6; % Sampling frequency in Hz (100 MHz)
c = 1540; % Speed of sound in m/s (1540 m/s for soft tissue)
set_sampling(fs); % Set the sampling frequency in Field II
% Adjusted Parameters for Feasibility
lambda = c / f0; % Wavelength in meters
width = lambda / 2; % Element width set to ~λ/2 for optimal
performance
kerf = 6e-6; % Set kerf to 6 μm
% Calculate maximum number of elements that can fit within 1.5 mm
width
W_total = 1.5e-3; % Total width of the transducer in meters (1.5 mm)
N_elements = 1;
while width > 0.05e-3 % Ensure element width is at least 0.05 mm for
feasibility
N_elements = N_elements + 1;
width = (W_total - (N_elements - 1) * kerf) / N_elements;
end
N_elements = N_elements - 1; % Reduce by 1 to ensure the last feasible
value
width = (W_total - (N_elements - 1) * kerf) / N_elements;
height = 1.5e-3; % Element height in meters (1.5 mm)
focus = [0 0 15e-3]; % Focus at 15 mm depth (in meters)
```

```matlab
curve_radius = 20e-3; % Radius of curvature in meters (20 mm)
matching_layer_thickness = 0.02e-3; % Reduced matching layer thickness
in meters (20 microns)
matching_layer_speed = 2000; % Speed of sound in matching layer
material (2000 m/s)
% Checkpoint: Print parameters to verify setup
disp('--- Step 1: Transducer Parameters Setup ---');
disp(['Transducer Frequency (f0): ', num2str(f0/1e6), ' MHz']);
disp(['Sampling Frequency (fs): ', num2str(fs/1e6), ' MHz']);
disp(['Speed of Sound (c): ', num2str(c), ' m/s']);
disp(['Element Dimensions: ', num2str(width*1e3), ' mm x ',
num2str(height*1e3), ' mm']);
disp(['Number of Elements (N_elements): ', num2str(N_elements)]);
disp(['Focus Depth: ', num2str(focus(3)*1e3), ' mm']);
disp(['Kerf Size: ', num2str(kerf*1e6), ' µm']); % Display kerf in
microns
disp(['Matching Layer Thickness: ',
num2str(matching_layer_thickness*1e3), ' mm']);
disp(['Speed of Sound in Matching Layer: ',
num2str(matching_layer_speed), ' m/s']);
% Create a curved linear array transducer using the Field II function
Th = xdc_convex_array(N_elements, width, height, kerf, curve_radius,
1, 1, focus);
% Set impulse response with matching layer effects
impulse_response = sin(2 * pi * f0 * (0:1/fs:2/f0)); % Basic impulse
response
matching_layer_delay = matching_layer_thickness /
matching_layer_speed; % Delay introduced by matching layer
impulse_response = [zeros(1, round(matching_layer_delay * fs)),
impulse_response]; % Add delay to simulate matching layer
```

```matlab
impulse_response = impulse_response .*
hann(length(impulse_response))'; % Apply a Hann window to smooth the
impulse response
xdc_impulse(Th, impulse_response);
% Set amplified excitation for the transducer
excitation = 30 * sin(2 * pi * f0 * (0:1/fs:2/f0)); % Amplified
excitation signal by factor of 30
xdc_excitation(Th, excitation);
% Apply Chebyshev apodization to reduce side lobe levels and improve
CNR
apodization = chebwin(N_elements, 30)'; % Chebyshev window with -30 dB
side lobe level
xdc_apodization(Th, 0, apodization);
% Checkpoint: Confirm transducer setup is complete
disp('Transducer successfully created with curved array geometry,
matching layer effects, and amplified impulse/excitation set!');
% Step 2: Define Phantom and Tissue Properties
% Set tissue medium properties
set_field('c', 1540); % Speed of sound for tissue (m/s)
% Define detailed anatomical structures for the ampulla of Vater,
duodenal papilla, biliary duct, and pancreatic duct
ampulla_positions = [0, 0, 15e-3; 0.5e-3, 0, 15.5e-3; -0.5e-3, 0,
15.5e-3];
biliary_duct_positions = [1e-3, 0, 16e-3; -1e-3, 0, 16e-3; 0, 0,
16.5e-3];
pancreatic_duct_positions = [0, 1e-3, 17e-3; 0, -1e-3, 17e-3; 0.5e-3,
0.5e-3, 17.5e-3];
% Combine all scatterer positions
phantom_positions = [ampulla_positions; biliary_duct_positions;
pancreatic_duct_positions];
```

```matlab
% Assign reflectivity values to different anatomical structures
ampulla_amplitudes = [1; 0.9; 0.9]; % Higher reflectivity for ampulla
biliary_duct_amplitudes = [0.8; 0.8; 0.75]; % Reflectivity for biliary
duct
pancreatic_duct_amplitudes = [0.85; 0.85; 0.8]; % Reflectivity for
pancreatic duct
% Combine all scatterer amplitudes
phantom_amplitudes = [ampulla_amplitudes; biliary_duct_amplitudes;
pancreatic_duct_amplitudes];
% Create scatterers for the phantom
phantom_handle.positions = phantom_positions;
phantom_handle.amplitudes = phantom_amplitudes;
% Step 3: Perform Pulse-Echo Simulations Across Phantom Model
% Define scan points
xpoints = (-5:0.1:5) * 1e-3; % Lateral points in meters (-5 mm to 5
mm)
zpoints = (10:0.5:25) * 1e-3; % Depth points from 10 mm to 25 mm in
meters
% Initialize matrix for storing beam profile results
beam_profiles = zeros(length(zpoints), length(xpoints));
% Pulse-Echo Simulation Loop
for z_idx = 1:length(zpoints)
[RF_data, ~] = calc_hhp(Th, phantom_handle, [xpoints; zeros(1,
length(xpoints)); zpoints(z_idx) * ones(1, length(xpoints))]');
beam_profiles(z_idx, :) = max(abs(RF_data), [], 1); % Store the
maximum values for each depth
end
% Step 4: Visualize the Simulated Pulse-Echo Results
% 3D Visualization of Beam Profile Across the Phantom
figure;
```

```matlab
[X, Z] = meshgrid(xpoints * 1e3, zpoints * 1e3); % Convert to mm for
plotting
mesh(X, Z, beam_profiles);
xlabel('Lateral distance [mm]');
ylabel('Depth [mm]');
zlabel('Intensity');
title('3D Visualization of Pulse-Echo Beam Profile Across Phantom');
colorbar;
disp('--- Step 4: Pulse-Echo Results Visualization Completed ---');
% Step 5: Calculate and Visualize SNR and CNR
% Signal Region (Assuming central region is the signal)
signal_region = beam_profiles(15:20, 20:40); % Select a region for
signal
signal_mean = mean(signal_region(:));
signal_std = std(signal_region(:));
% Noise Region (Assuming edges are noise)
noise_region = beam_profiles(1:5, 1:10); % Select a region for noise
noise_mean = mean(noise_region(:));
noise_std = std(noise_region(:));
% Calculate SNR
SNR = 20 * log10(signal_mean / noise_std);
disp(['Signal-to-Noise Ratio (SNR): ', num2str(SNR), ' dB']);
% Contrast Region (Assuming a different depth)
contrast_region = beam_profiles(25:30, 20:40); % Select a region for
contrast
contrast_mean = mean(contrast_region(:));
% Calculate CNR
CNR = 20 * log10(abs(signal_mean - contrast_mean) / noise_std);
disp(['Contrast-to-Noise Ratio (CNR): ', num2str(CNR), ' dB']);
% Visualize SNR and CNR Regions
```

```matlab
figure;
imagesc(xpoints * 1e3, zpoints * 1e3, beam_profiles);
xlabel('Lateral distance [mm]');
ylabel('Depth [mm]');
title('SNR and CNR Regions Visualization');
colorbar;
hold on;
rectangle('Position', [xpoints(20)*1e3, zpoints(15)*1e3, (xpoints(40)-
xpoints(20))*1e3, (zpoints(20)-zpoints(15))*1e3], 'EdgeColor', 'g',
'LineWidth', 2); % Signal region
txt1 = text(xpoints(40)*1e3, zpoints(20)*1e3, ' Signal', 'Color',
'g');
rectangle('Position', [xpoints(1)*1e3, zpoints(1)*1e3, (xpoints(10)-
xpoints(1))*1e3, (zpoints(5)-zpoints(1))*1e3], 'EdgeColor', 'r',
'LineWidth', 2); % Noise region
txt2 = text(xpoints(10)*1e3, zpoints(5)*1e3, ' Noise', 'Color', 'r');
rectangle('Position', [xpoints(20)*1e3, zpoints(25)*1e3, (xpoints(40)-
xpoints(20))*1e3, (zpoints(30)-zpoints(25))*1e3], 'EdgeColor', 'b',
'LineWidth', 2); % Contrast region
txt3 = text(xpoints(40)*1e3, zpoints(30)*1e3, ' Contrast', 'Color',
'b');
hold off;
disp('--- Step 5: SNR and CNR Calculation Completed ---');
% Step 6: Simulated Pulse-Echo Image at 15 mm Focus Depth
focus_depth = 15e-3;
[RF_data, start_time] = calc_hhp(Th, phantom_handle, [xpoints;
zeros(1, length(xpoints)); focus_depth * ones(1, length(xpoints))]');
beam_profile = abs(RF_data); % Take the envelope of the RF data
% Generate and visualize Pulse-Echo Image
figure;
```

```matlab
imagesc(xpoints * 1e3, ((0:size(RF_data, 1)-1) / fs + start_time) * c
/ 2 * 1e3, beam_profile);
xlabel('Lateral distance [mm]');
ylabel('Depth [mm]');
title('Simulated Pulse-Echo Image at 15 mm Focus Depth');
colorbar;
colormap(gray);
disp('--- Step 6: Pulse-Echo Image Generated ---');
% Step 7: Beam Analysis at -6 dB Level
[max_value, max_depth_idx] = max(beam_profile(:)); % Find the maximum
value and its index
[row_idx, col_idx] = ind2sub(size(beam_profile), max_depth_idx); % Get
row and column indices for max value
half_max = max_value / sqrt(2); % -6 dB level
% Lateral beam width at -6 dB
lateral_profile = beam_profile(row_idx, :);
lateral_positions = find(lateral_profile >= half_max);
if ~isempty(lateral_positions)
lateral_width = (max(lateral_positions) - min(lateral_positions)) *
0.1; % Convert index difference to mm
else
lateral_width = NaN;
end
% Axial beam width at -6 dB
axial_profile = beam_profile(:, col_idx);
axial_positions = find(axial_profile >= half_max);
if ~isempty(axial_positions)
axial_width = (max(axial_positions) - min(axial_positions)) * (1 / fs)
* c / 2 * 1e3; % Convert index difference to mm
else
```

```matlab
    axial_width = NaN;
end
% Display beam analysis results
disp('--- Step 7: Beam Analysis at -6 dB Level ---');
disp(['Lateral Beam Width (-6 dB): ', num2str(lateral_width), ' mm']);
disp(['Axial Beam Width (-6 dB): ', num2str(axial_width), ' mm']);
% Step 8: Energy Distribution Visualization
energy_distribution = sum(beam_profiles, 2);
figure;
plot(zpoints * 1e3, energy_distribution, '-o');
xlabel('Depth [mm]');
ylabel('Integrated Energy [a.u.]');
title('Energy Distribution along Depth for Pulse-Echo Beam Profile');
grid on;
% Find and display peak integrated energy depth
[peak_energy, peak_idx] = max(energy_distribution);
peak_depth = zpoints(peak_idx) * 1e3; % Convert to mm
disp(['Peak Integrated Energy Depth: ', num2str(peak_depth), ' mm']);
disp('--- Step 8: Energy Distribution Analysis Completed ---');
% Step 9: Point Spread Function (PSF) Calculation
% Define a single point scatterer at the focus
psf_position = [0, 0, focus(3)];
psf_amplitude = 1;
% Create scatterer for PSF calculation
psf_handle.positions = psf_position;
psf_handle.amplitudes = psf_amplitude;
% Define scan points for PSF analysis (lateral and axial)
psf_xpoints = (-5:0.05:5) * 1e-3; % Lateral points in meters (-5 mm to
5 mm) for finer resolution
```

```matlab
psf_zpoints = (focus(3) - 5e-3:0.1e-3:focus(3) + 5e-3); % Axial points
around focus depth (15 mm)
% Initialize matrix for storing PSF beam profile results
psf_profiles = zeros(length(psf_zpoints), length(psf_xpoints));
% Pulse-Echo Simulation Loop for PSF
for z_idx = 1:length(psf_zpoints)
[RF_psf_data, ~] = calc_hhp(Th, psf_handle, [psf_xpoints; zeros(1,
length(psf_xpoints)); psf_zpoints(z_idx) * ones(1,
length(psf_xpoints))]');
psf_profiles(z_idx, :) = max(abs(RF_psf_data), [], 1); % Store the
maximum values for each depth
end
% PSF Metrics Calculation
max_value = max(psf_profiles(:));
half_max = max_value / sqrt(2); % -6 dB level
% Lateral Resolution Calculation at Focus Depth (Z = 15 mm)
[~, focus_idx] = min(abs(psf_zpoints - focus(3))); % Find index
closest to focus depth
lateral_profile = psf_profiles(focus_idx, :);
lateral_positions = find(lateral_profile >= half_max);
if ~isempty(lateral_positions)
lateral_resolution = (max(lateral_positions) - min(lateral_positions))
* 0.05; % Convert index difference to mm
else
lateral_resolution = NaN;
end
% Axial Resolution Calculation at Focus (X = 0)
[~, center_idx] = min(abs(psf_xpoints)); % Find index closest to
lateral center
axial_profile = psf_profiles(:, center_idx);
```

```matlab
axial_positions = find(axial_profile >= half_max);
if ~isempty(axial_positions)
axial_resolution = (max(axial_positions) - min(axial_positions)) *
0.1; % Convert index difference to mm
else
axial_resolution = NaN;
end
% Display PSF Analysis Results
disp('--- Step 9: PSF Analysis ---');
disp(['Lateral Resolution from PSF: ', num2str(lateral_resolution), '
mm']);
disp(['Axial Resolution from PSF: ', num2str(axial_resolution), '
mm']);
% Visualize PSF in Lateral, Axial, and 3D
figure;
% Lateral Profile at Focus Depth
subplot(3, 1, 1);
plot(psf_xpoints * 1e3, lateral_profile);
xlabel('Lateral distance [mm]');
ylabel('Intensity [a.u.]');
title('Point Spread Function (PSF) - Lateral Profile at Focus Depth');
grid on;
% Axial Profile at Center Position
subplot(3, 1, 2);
plot(psf_zpoints * 1e3, axial_profile);
xlabel('Depth [mm]');
ylabel('Intensity [a.u.]');
title('Point Spread Function (PSF) - Axial Profile at Center
Position');
grid on;
```

```matlab
% 3D PSF Visualization
subplot(3, 1, 3);
[X_psf, Z_psf] = meshgrid(psf_xpoints * 1e3, psf_zpoints * 1e3); % Convert to mm for plotting
mesh(X_psf, Z_psf, psf_profiles);
xlabel('Lateral distance [mm]');
ylabel('Depth [mm]');
zlabel('Intensity');
title('3D Point Spread Function (PSF) at Focus Depth');
colorbar;
% Cleanup Field II after usage
xdc_free(Th); % Free the transducer memory
field_end; % End the Field II session
```